Giampaolo Martufi
Università degli Studi di Roma Tor Vergata,
Via del Politecnico,
1 00133 Roma Italia
e-mail: martufi@kth.se

Elena S. Di Martino
Department of Civil Engineering,
and Centre for Bioengineering Research and Education,
University of Calgary,
2500 University Drive Northwest,
Calgary, AL, T2N 1N4, Canada
e-mail: edimarti@ucalgary.ca

Cristina H. Amon
Department of Mechanical and Industrial Engineering,
University of Toronto,
5 King's College Road,
Toronto, ON, M5S 3G8, Canada
e-mail: cristina.amon@utoronto.ca

Satish C. Muluk
Division of Vascular Surgery,
Allegheny General Hospital,
320 East North Avenue,
South Tower, 14th Floor,
Pittsburgh, PA 15212-4772
e-mail: smuluk@wpahs.org

Ender A. Finol[1]
Department of Biomedical Engineering,
and Department of Mechanical Engineering,
Institute for Complex Engineered Systems,
Carnegie Mellon University,
Pittsburgh, PA 15213-3890
e-mail: finole@cmu.edu

Three-Dimensional Geometrical Characterization of Abdominal Aortic Aneurysms: Image-Based Wall Thickness Distribution

The clinical assessment of abdominal aortic aneurysm (AAA) rupture risk is based on the quantification of AAA size by measuring its maximum diameter from computed tomography (CT) images and estimating the expansion rate of the aneurysm sac over time. Recent findings have shown that geometrical shape and size, as well as local wall thickness may be related to this risk; thus, reliable noninvasive image-based methods to evaluate AAA geometry have a potential to become valuable clinical tools. Utilizing existing CT data, the three-dimensional geometry of nine unruptured human AAAs was reconstructed and characterized quantitatively. We propose and evaluate a series of 1D size, 2D shape, 3D size, 3D shape, and second-order curvature-based indices to quantify AAA geometry, as well as the geometry of a size-matched idealized fusiform aneurysm and a patient-specific normal abdominal aorta used as controls. The wall thickness estimation algorithm, validated in our previous work, is tested against discrete point measurements taken from a cadaver tissue model, yielding an average relative difference in AAA wall thickness of 7.8%. It is unlikely that any one of the proposed geometrical indices alone would be a reliable index of rupture risk or a threshold for elective repair. Rather, the complete geometry and a positive correlation of a set of indices should be considered to assess the potential for rupture. With this quantitative parameter assessment, future research can be directed toward statistical analyses correlating the numerical values of these parameters with the risk of aneurysm rupture or intervention (surgical or endovascular). While this work does not provide direct insight into the possible clinical use of the geometric parameters, we believe it provides the foundation necessary for future efforts in that direction. [DOI: 10.1115/1.3127256]

Keywords: aortic pathology, computed tomography, image-based modeling, curvature, finite element meshing, segmentation, reconstruction, shape, biomechanics

1 Introduction

An aneurysm is defined as a local permanent dilatation of an artery at least 1.5 times its normal diameter. While any artery can become aneurysmal, the infrarenal segment of the abdominal aorta is a common site for the development of aneurysms. The conventional definition of abdominal aortic aneurysm (AAA) is a diameter of the infrarenal aorta greater than 30 mm. The incidence of AAA is 2–4% in the adult population, and it is growing with increase in the average population age. AAA rupture is responsible for an estimated 15,000 deaths per year and it is considered the 13th most common cause of death in the United States [1,2]. Aneurysms are, for the most part, asymptomatic, and may rupture at any point in time, regardless of their size or age of the pathology. Consequently, one of the most challenging issues in clinical management of known aneurysm patients is the evaluation of the patient-specific risk of aneurysm rupture at any given time. Commonly used "risk predictors," are the maximum transverse diameter of an aneurysm and its expansion rate. In particular, a maximum diameter of 55 mm and an expansion rate of 1 cm/year are generally used as thresholds to recommend elective repair [3]. Traditional aneurysm repair, by open surgical treatment, is associated with high morbidity and a mortality rate ranging between 2% and 4% [4,5]. As an alternative to surgical resection, the use of endovascular grafts allows surgeons to repair aneurysms by delivering a bypass graft through a small incision in the femoral artery. If left untreated, all AAAs progress toward further enlargement and eventually will rupture though there are no available indicators of how close rupture is and for selected patients rupture may not occur during their lifetime. AAA rupture is a biomechanical phenomenon that occurs when the mechanical stress acting on the aneurysm inner wall due to intraluminal pressure, exceeds the failure strength of the degenerated aortic tissue [6].

Recent studies [7,8] show that peak wall stress in AAAs is a more reliable parameter than maximum transverse diameter for aneurysm rupture prediction. In fact, the peak wall stress for ruptured aneurysms is about 60% higher than for nonruptured and the location of the maximum wall stress correlates with the site of rupture [8]. Wall stress is associated with the aneurysm geometry [6], making it relevant to compute geometric parameters from diagnostic images. However, it is necessary to underline that wall stress alone is not sufficient to predict rupture risk; regional estimations of wall strength would also be necessary [9]. In fact, the degeneration of aortic wall connective tissue should be taken into consideration. Destruction of elastin and collagen in the media

[1]Corresponding author.

Contributed by the Bioengineering Division of ASME for publication in the JOURNAL OF BIOMECHANICAL ENGINEERING. Manuscript received September 10, 2008; final manuscript received December 25, 2008; published online May 12, 2009. Review conducted by Michael Sacks.

and adventitia causes a significant loss of structural integrity of the aortic wall [10], thereby increasing the risk of rupture of an individual aneurysm, when all other factors are the same. Other risk factors, including hypertension, atherosclerosis, smoking, and a positive family history, may influence the imbalance of the cellular and extracellular matrix homeostases, resulting in the thinning and weakening of the aortic wall.

The presence of intraluminal thrombus, which forms because of disturbed blood flow and blood stagnation, has an effect both on the aortic wall degeneration and on the maximum peak wall stresses in the AAA [11]. An autopsy study [12] demonstrated that ruptured aneurysms present a larger maximum transverse diameter and thicker thrombus in comparison to unruptured aneurysm, showing a positive correlation between aneurysm size, thrombus thickness, and rupture risk. On the other hand, the same study demonstrated that ruptured aneurysms more often presented a fusiform shape, rather than spherical, indicating that shape, and not size alone, influences rupture risk.

Several authors have used shape measures in the characterization of disease processes. Early studies report on the power of shape measures to distinguish between normal and abnormal brain surface shapes and to establish a relationship between the shape of the surface of the human brain and the function of the underlying tissue [13]. A recent study describes the derivation of a set of global indices for the size and shape of cerebral aneurysms for assessment of their rupture potential and for choosing the appropriate clinical treatment modality [14,15]. A quantitative tortuosity index has been recently proposed to quantify AAA shape as a function of the orthographic projection of the aortic centerline about its central axis [16].

Ruptured AAAs seem to be less tortuous and have a larger cross-sectional diameter asymmetry [17], which is consistent with finite element studies showing that the highest wall stress is obtained in AAAs with an asymmetric geometry [6,7]. In addition, Finol et al. [18] demonstrated that asymmetry in idealized shaped AAAs increases the maximum wall shear stress at peak flow and induces secondary flows in late diastole. The evidence for geometric asymmetry is further supported by the finding that peak wall stress is localized near the aorta-aneurysm inflection point where the aneurysm curvature changes [19] Moreover, the location of maximum stress at the posterior wall seems to coincide with peaks in the magnitude of the Gaussian curvature [20].

A factor of significant importance in AAA rupture risk prediction is the nonuniformity of the wall thickness. Di Martino et al. [21], using a laser micrometer, measured the thickness of AAA wall specimens, obtained fresh from the operating room from patients undergoing surgical repair. A significant difference was found in wall thickness between ruptured (3.6 ± 0.3 mm) and electively repaired (2.5 ± 0.1 mm) aneurysms, as well as an inverse correlation between wall thickness and local tissue strength. In an autopsy study, Rhagavan et al. [22] analyzed the tissue properties of three unruptured and one ruptured AAA revealing that all aneurysms had considerable regional variation in wall thickness and there was a significant reduction in wall thickness near the rupture site. Similarly, Mower et al. [23] demonstrated that the wall thickness represents a major parameter influencing wall stress distribution, rather than aneurysm sac maximum diameter alone. To this end, fluid-structure interaction simulations of AAA models [24] showed that the assumption of constant distribution of wall thickness causes an underestimation of the maximum wall stress of up to 77% when compared with nonuniform wall thickness geometry. In addition, Scotti and co-workers [24–26] confirmed that aneurysm asymmetry and wall thickness play an important role in the estimation of peak wall stress; in particular nonhomogenous wall thickness yields a maximum Von Mises stress of up to four times higher than the same model analyzed with uniform wall thickness.

Due to the inability to measure wall thickness noninvasively, a uniform thickness of 1.5 mm is typically assumed in biomechanics modeling of AAAs [27]. Another significant limitation of many previous studies is the use of idealized aneurysm shapes. Realistic AAAs have complex, tortuous, and asymmetric shapes with local changes in surface curvature [28] and local changes in wall thickness. It is evident that an accurate characterization of the aneurysm shape and the variation of wall thickness need to be accounted for in the assessment of AAA rupture risk. Moreover, accurate reproductions of AAA geometries are necessary to customize endovascular grafts on a patient-specific basis.

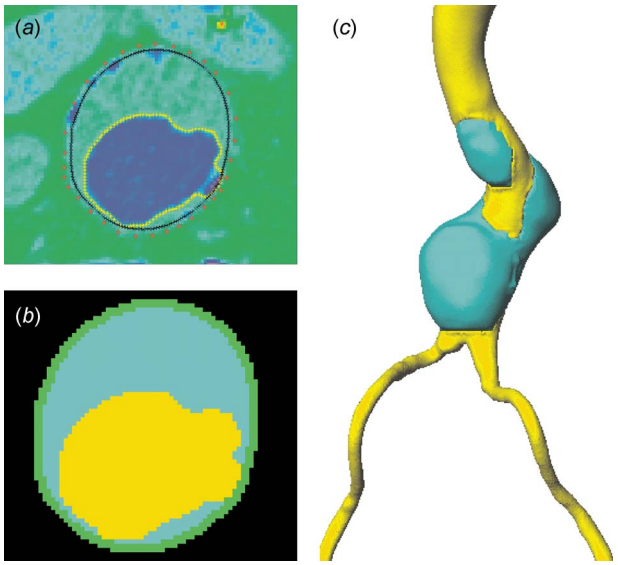

Fig. 1 3D image segmentation and model reconstruction: (*a*) active contour detection on image with false coloring, (*b*) mask generated from segmented image, and (*c*) resulting 3D aortic geometry (lumen shown in yellow and thrombus in cyan)

The objectives of this study are to use anatomically realistic abdominal aortic aneurysm models, originated from CT images, to derive and evaluate a set of global geometrical indices describing the size and shape of the aneurysm sac. Additionally, an estimation of local variation and distribution of AAA wall thickness is provided by means of an ad hoc image processing suite developed for cardiovascular structures.

2 Methods

The procedure for characterizing abdominal aortic aneurysm geometry includes two major steps: (i) image segmentation and wall thickness detection and (ii) computation of the size and shape indices. The digital imaging and communications in medicine (DICOM) images were imported into an in-house MATLAB based image segmentation code (VESSEG v.1.0.2, Carnegie Mellon University, Pittsburgh, Pennsylvania), for the lumen and outer wall segmentations, and wall thickness detection as illustrated in Fig. 1.

2.1 Image-Based Segmentation, Reconstruction and Meshing. The VESSEG suite of routines was written in MATLAB to provide portability and flexibility to the procedure [29]. A series of specific operations in the VESSEG suite enables segmentation of the lumen and outer wall of the vessel. Interaction with the user takes place through a user-friendly graphical user interface (GUI) that allows access to all code functions while hiding data structures from the user. Three different algorithms form the basis of the segmentation tool developed: *lumen segmentation*, *outer wall segmentation*, and *wall thickness detection*.

The lumen segmentation is based on the intensity gradient between the lumen and the surrounding structures and works best when the CT scanning procedure involves use of contrast medium. Due to the adequate gradient granted by the presence of

contrast medium in the lumen, the procedure calls for two simple operations: first, the user selects a sample point inside the lumen and the routine then proceeds to identify the boundary of the lumen by finding the decrease in intensity. The program verifies the segmentation of every slice subsequent to the first against an average of the previous segmentation and modifies the threshold used for the intensity when needed. As protection against possible errors, when a suitable value for the threshold cannot be found, the user can provide a threshold manually by selecting the boundary between the lumen and the wall.

The user may perform outer wall segmentation in two ways: manual or automatic; the user selects the best segmentation method on a case-by-case basis. The manual segmentation method accepts a cropped image where the usable area is reduced by only considering areas close to the lumen and applies a series of operations, including smoothing filters and contour functions, to generate an array of contours or isolines of the image intensity. The routine provides a selection of possible contours for the user to make a choice. For the automatic segmentation method, the user must select an intensity threshold used to create a list of boundaries. The boundary that is closest to the lumen without crossing it and that extends completely around the lumen is the likely boundary. Additional control rules embedded in the routine assure that the segmentation of the slice is discarded when no possible boundaries can be created and that the threshold is changed accordingly to attempt a new segmentation.

Our algorithm for wall thickness detection is based on the image texture variation across the different structures of the aorta. In brief, flat-fielding is used at the outset to enhance contrast in the input image and subsequently the image is processed in parallel by a segmentation routine that uses intensity histograms and a neural network. Highlights of our method are the use of a background homogenization function and of an ad hoc cropping function that reduces the area to be processed to a narrow annularlike region around the already segmented lumen region. The neural network is trained by extracting samples of the background, thrombus, and lumen regions, which are used to build the feature vectors necessary for the neural network process. Both intensity-based features of the image (mean, standard deviation, and interquartile range), as well as image texture features (such as mean, standard deviation, energy, and homogeneity of the gray-level co-occurrence matrix) are used by the neural network. Because of this process, two ternary images—segmenting the image in background, thrombus, and lumen regions—are created; one obtained from the intensity histogram algorithm and one from the neural network. The neural network produces an "inclusive" thrombus image, i.e., it contains anything in the "aneurysm" area, including thrombus and the wall. The histogram produces a more conservative thrombus image, only including structures that are definitively thrombus, excluding the wall. Subtracting the two ternary images creates a rough wall image. The process is then refined by inspecting which parts of the rough wall fall in regions of detectable thickness. Only points that are deemed acceptable by the algorithm are included in the wall thickness detection. Finally, smoothing and 3D interpolation algorithms assign wall thickness values to the entire vessel. The output of the wall detection algorithm is a set of thickness values for each of 72 points (every -5 deg.) located on the inner wall on each longitudinal slice.

The segmented lumen and inner wall for all the aneurysms are exported from VESSEG as a set of *mask images* that are used in ScanIP (Simpleware Ltd., Exeter, U.K.) to create the lumen and inner wall surfaces as stereolithography (STL) models. Rhinoceros (McNeel, Seattle, WA) is utilized to complete the reconstruction process with smoothing. The smoothed STLs of the lumen and the inner wall are imported into ScanCAD (Simpleware Ltd., Exeter, U.K.) where a voxelization process is performed to generate the final masks for the inner wall and lumen. The AAA sac is isolated from the fully reconstructed geometry to calculate the proposed geometrical parameters. To this end, and in the remainder of this manuscript, the sac comprises the entire dilated infrarenal aorta proximal to and excluding the iliac bifurcation. An in-house code written in MATLAB as an adjunct to VESSEG is used to calculate semi-automatically all size and shape indices. Finite element meshing of the arterial wall is performed in ScanFE (Simpleware Ltd., Exeter, UK) using three-node shell elements with five integration points across the shell. The meshes, ranging in size from 80,000 to 240,000 nodes, are used only for the calculation of the curvature-based indices.

2.2 One-Dimensional Size Indices. Nine 1D size indices were defined: maximum transverse diameter ($D_{\max}$), two neck diameters (D_{neck1} and D_{neck2}), abdominal height (H), length of centerline from neck to distal end of AAA (L), length of neck centerline (L_{neck}), the bulge height (H_b), and the distance between the lumen centroid and the centroid of the cross section where $D_{\max}$ is located (d_c).

$D_{\max}$ is the maximum transverse diameter for all cross sections within the AAA sac. D_{neck1} is the proximal neck diameter immediately below the renal arteries; if no neck is present, it is calculated as the smallest diameter distal to the renal arteries. D_{neck2} is the distal neck diameter. H_b is the perpendicular distance from the cross section where $D_{\max}$ is measured to the cross section where D_{neck1} is measured. Since typically arterial cross sections are noncircular in shape, the definition used for calculating $D_{\max}$, D_{neck1}, and D_{neck2} is the fluid mechanics definition for hydraulic diameter as follows:

$$D_i = \frac{4A_i}{P_i} \tag{1}$$

where A_i is the cross-sectional area and P_i is the perimeter of the same cross section. Figure 2 illustrates the 1D indices and their location after segmentation of the AAA model.

2.3 Two-Dimensional Shape Indices. Six 2D shape indices were derived from the 1D size measurements: diameter-height ratio (DHr), diameter-diameter ratio (DDr), height ratio (Hr), bulge location (BL), asymmetry factor (β), and tortuosity (T). These indices are defined as follows in Eqs. (2)–(7):

$$\text{DHr} = \frac{D_{\max}}{H} \tag{2}$$

$$\text{DDr} = \frac{D_{\max}}{D_{\text{neck1}}} \tag{3}$$

$$\text{Hr} = \frac{H}{H_{\text{neck}}} \tag{4}$$

$$\text{BL} = \frac{H_b}{H} \tag{5}$$

$$\beta = 1 - \frac{d_c}{D_{\max}} \tag{6}$$

$$T = \frac{L}{d} \tag{7}$$

where d is the Euclidean distance from the centroid of the cross section where D_{neck1} is located to the centroid of the cross section at the AAA distal end.

DHr is an expression of the fusiform shape of the AAA sac. BL and Hr represent two normalized heights. While BL provides a measure of the relative position of the maximum transverse dimension with respect to the neck, Hr is an assessment of the relative neck height in comparison with the AAA height. β and T

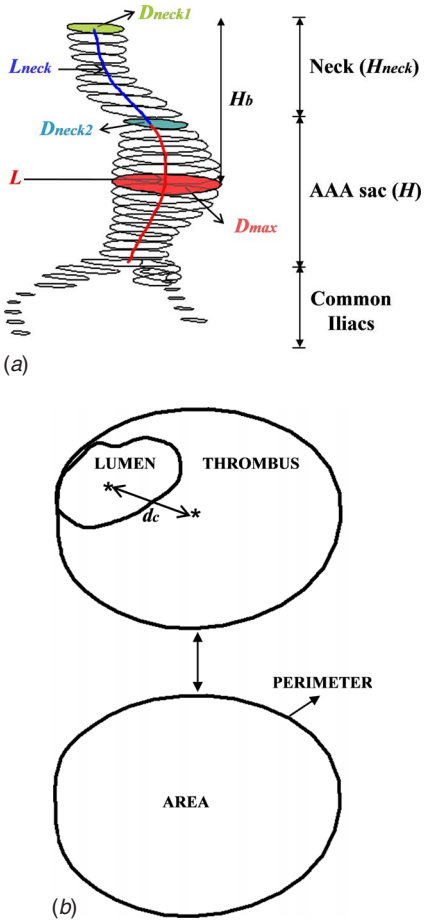

Fig. 2 Schematic of the 1D geometrical indices: (*a*) diameters, lengths and heights in a segmented AAA model; and (*b*) location of d_c and parameters required to calculate a cross-sectional diameter A_i

indicate the degree of AAA sac asymmetry and the tortuosity of the aneurysmal aorta, respectively. Table 1 provides a schematic of the 2D shape indices.

2.4 Three-Dimensional Size Indices. The luminal AAA volume (V) and the luminal surface area of the AAA sac (S) have been computed directly with the VESSEG code. In the present work, two intraluminal thrombus (ILT)-related indices are proposed: (i) the volume of intraluminal thrombus contained within the AAA sac, computed according to the aforementioned approach of subtracting the lumen volume from the inner wall volume, and (ii) γ, the ratio of AAA ILT volume defined as

$$\gamma = \frac{V_{\mathrm{ILT}}}{V} \tag{8}$$

2.5 3D Shape Indices. The isoperimetric ratio (IPR) and nonfusiform index (NFI) are two 3D shape indices based on luminal volume and surface area of the AAA sac. IPR is the nondimensional ratio of the luminal surface area to the volume of the sac and represents a quantification of the degree of folding of the surface area. This measure is independent of size changes as it shows the increase in contained surface area. IPR is defined as [13,14]

$$\mathrm{IPR} = \frac{S}{V^{2/3}} \tag{9}$$

Table 1 Schematic illustrations of 2D shape indices providing an approximate measure to construe the global AAA shape

2D Shape Index	Low	High
DHr	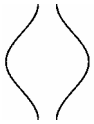	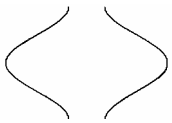
DDr	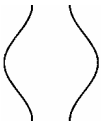	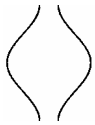
Hr	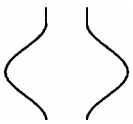	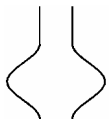
BL	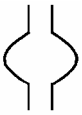	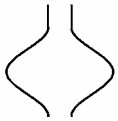
β	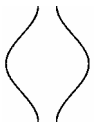	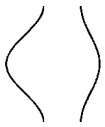
T	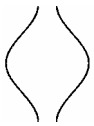	

Based on the patient-specific neck diameter, maximum AAA diameter, and height of the aneurysm sac, an idealized fusiform aneurysm was modeled following the equation proposed by Finol and Amon [30]:

$$r(z) = \left(\frac{D_{\max} - D_{\mathrm{neck2}}}{4}\right)\left[1 + \sin\left(\frac{2\pi z}{H} - \frac{\pi}{2}\right)\right] + \frac{D_{\mathrm{neck2}}}{2}$$

$$0 \le z \le H \tag{10}$$

The corresponding volume (V_{fusiform}) and surface area (S_{fusiform}) of this idealized aneurysm are computed to calculate NFI, which is defined as

$$\mathrm{NFI} = 1 - \left(\frac{V_{\mathrm{fusiform}}^{2/3}}{S_{\mathrm{fusiform}}}\right)\left(\frac{S}{V^{2/3}}\right) \tag{11}$$

This index varies from 0 to 1; it is equal to 0 for a fusiform-shaped aneurysm and increases to 1 with deviation from a fusiform shape. The deviation in shape can originate from the presence of asymmetry and tortuosity in the AAA sac.

2.6 Second-Order Curvature-Based Indices. The second-order indices are curvature-based and involve the second derivative of the nodal positions of the AAA mesh [14]. To estimate the distribution of local curvatures at node i on the triangulated surface of the geometric model, a local orthogonal coordinate system (u_1, u_2, n) is established, where n is the unit normal vector at the ith node and u_1 and u_2 are unit vectors contained in the tangent plane at node i. The normal $\boldsymbol{n}$ is initially computed for each triangular element after which an approximate normal n at the ith node is estimated using the weighted average of unit normals of

all adjacent triangular elements, using the element areas as the weights. The first unit basis vector u_1 is calculated choosing a unit vector perpendicular to n and in the tangent plane at node i, while u_2 is computed as the cross product of n and u_1 at the ith node. Given that

$$n = \begin{matrix} x_n \\ y_n \\ z_n \end{matrix}$$

u_1 is computed as follows:

$$\text{if } x_n \neq 0, \text{ then } \bar{u}_1 = \begin{matrix} -\dfrac{z_n + y_n}{x_n} \\ 1 \\ 1 \end{matrix}$$

$$\text{if } x_n = 0 \text{ and } y_n \neq 0, \text{ then } \bar{u}_1 = \begin{matrix} 1 \\ -\dfrac{z_n}{y_n} \\ 1 \end{matrix}$$

$$\text{if } x_n = 0, \; y_n = 0, \text{ and } z_n \neq 0, \text{ then } \bar{u}_1 = \begin{matrix} 1 \\ 1 \\ 1 \end{matrix}$$

and

$$u_1 = \frac{\bar{u}_1}{\|\bar{u}_1\|}$$

After defining this orthonormal coordinate system with the ith node at its origin, the node i and its directly connected nodes (neighboring nodes) are fit to a quadratic surface patch, using a bivariate polynomial $p(u,v)$ of the second-order expressed in the local coordinate system [31] as follows

$$p(u,v) = c_1 u^2 + c_2 uv + c_3 v^2 \tag{12}$$

where c_1, c_2, and c_3 are constants computed for the ith node in the local coordinate system defined by u_1 and u_2.

The Gauss–Weingarten map for this surface patch is defined as

$$G = 2\begin{pmatrix} c_1 & c_2 \\ c_2 & c_3 \end{pmatrix}$$

Therefore, the two principal curvatures k_1 and k_2 at the ith node are the eigenvalues of the matrix G and are computed explicitly using [31]

$$k_1 = c_1 + c_3 + \sqrt{(c_1 - c_3) + 4c_2^2} \tag{13}$$

$$k_2 = c_1 + c_3 - \sqrt{(c_1 - c_3) + 4c_2^2} \tag{14}$$

Using this approach, the two principal curvatures at all nodes of the triangulated aneurysm sac surface are determined. From the principal curvatures, the mean (M) and Gaussian curvatures (K) for each node are computed as

$$M = \frac{k_1 + k_2}{2} \tag{15}$$

$$K = k_1 k_2 \tag{16}$$

The AAA is a complex surface and even after a smoothing operation of the model, small surface irregularities will often remain. These irregularities in the surface will lead to large variations in the principal curvatures, making them difficult to interpret. Therefore, the principal curvatures and the normal vectors at the ith node were refined, as illustrated in Fig. 3, and made more consistent with the adjoining nodes [14]. The magnitude of the principal curvature and the normal at each node i are updated and refined by replacing them with the robust (resistant to outliers) locally weighted least-squares fit of the principal curvatures and the normal predicted using the aforementioned approach. The magnitude at the neighboring nodes was used to control the level of smoothing, and the two principal curvatures at the boundaries of the geometry were not considered in these calculations.

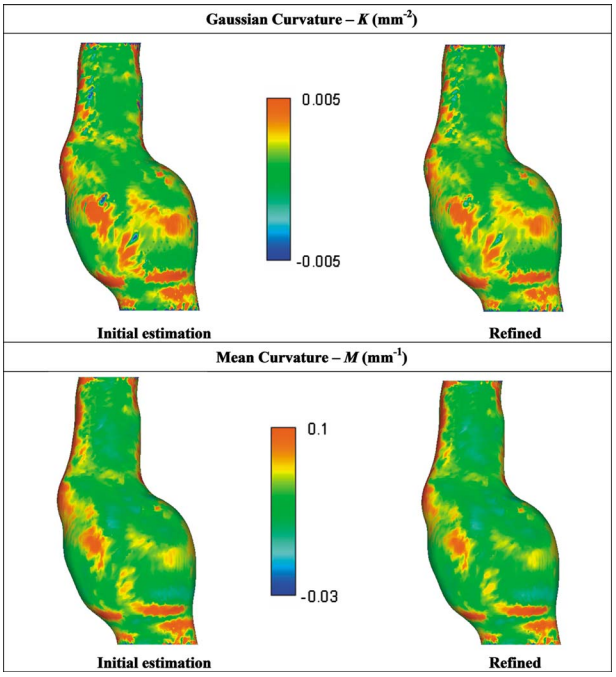

Fig. 3 Curvature refinement (Gaussian and mean) for model U1

The Gaussian and mean curvatures at each node give an indication of the local shape of the surface, in particular, $K>0$ indicates an elliptical surface, $K<0$ is hyperbolic (saddle points), while if $M>0$ the local region is more convex and for $M<0$ it is more concave. To obtain a global index that can entirely describe the curvature surface for the aneurysm sac, K and M averaged or integrated over the entire surface area has been proposed in literature [13,14,32]. Specifically, GAA [L^{-2}] and MAA [L^{-1}], the area-averaged Gaussian and mean curvatures [12,29], depend on the shape and size of the aneurysm, while the nondimensional GLN and MLN (the L2-norms of K and M, respectively [13,14]) are dependent on the surface shape and represent measures of irregularities on the AAA surface. These four global indices are calculated using all the nodes that are not on the proximal and distal boundaries of the AAA surface using

$$\text{GAA} = \frac{\sum_{\text{all elements}} K_j S_j}{\sum_{\text{all elements}} S_j} \tag{17}$$

$$\text{MAA} = \frac{\sum_{\text{all elements}} M_j S_j}{\sum_{\text{all elements}} S_j} \tag{18}$$

$$\text{GLN} = \frac{1}{4\pi}\sqrt{\sum_{\text{all elements}} S_j \cdot \sum_{\text{all elements}} (K_j^2 S_j)} \tag{19}$$

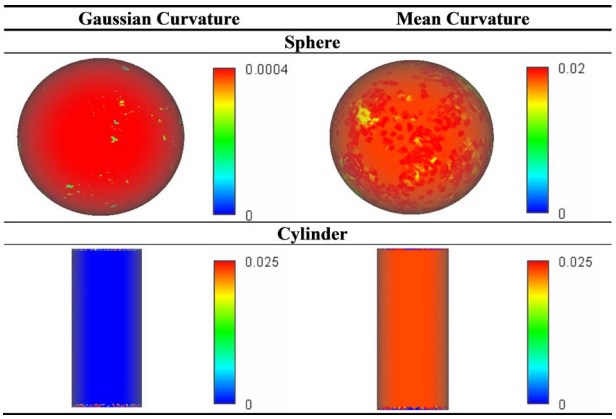

Fig. 4 Gaussian and mean curvatures for a sphere and cylinder predicted numerically (by VESSEG)

$$\mathrm{MLN} = \frac{1}{4\pi}\sqrt{\sum_{\text{all elements}} (M_j^2 S_j)} \tag{20}$$

where K_j and M_j are the Gaussian and mean curvatures associated with the jth triangular shell of the surface mesh, defined as the average Gaussian and Mean curvatures computed on the three shell nodes, and S_j is the surface area of the jth triangular shell.

3 Results

3.1 Validation of Size and Shape Indices. All size and shape indices are calculated from the segmented CT images; the finite element meshes are used only to compute the second-order curvature-based indices. Therefore, it is sufficient to validate the segmentation capabilities of VESSEG to provide confidence in the evaluation of the size and shape indices. We have previously calculated the interobserver variability and the reproducibility of our segmentation code based on 20 AAA CT image data sets (10 ruptured and 10 unruptured aneurysms), statistically analyzing the outcome of the lumen and outer wall segmentation algorithms of two double-blinded users [29]. Reproducibility and repeatability of the lumen segmentation algorithm were determined by comparing manual tracings made by the observers to contours generated automatically by the algorithm. For the lumen area measurement there was a high correspondence between the automatic and manual segmentations ($r=0.955$ and $r=0.958$ for ruptured and unruptured aneurysms, respectively) and between the manual segmentations of the users ($r=0.983$ and $r=0.966$ for ruptured and unruptured aneurysms, respectively). The outer wall segmentation also showed good agreement between the users with coefficients of variation ranging from 1.0% to 5.5% for the unruptured aneurysms [29].

3.2 Validation of Second-Order Curvature-Based Indices. To validate VESSEG for the computation of the Gaussian and mean curvatures, CAD models of a cylinder (diameter $D=40$ mm and height $H=100$ mm) and a sphere (radius $R=50$ mm) were generated and surface meshed with triangular shell elements. The sphere mesh consisted of 47,000 nodes while the cylinder mesh contained 17,000 nodes. It can be demonstrated analytically that $K=0$ and $M=1/D$ for a straight cylinder. Therefore, $K=0$ mm^{-2} and $M=0.025$ mm^{-1} are the basis of the VESSEG validation with respect to an idealized healthy artery with the aforementioned dimensions. For a sphere, $k_1=k_2=1/R$ and thus, $K=1/R^2$; also, $M=1/R$. Therefore, $K=0.0004$ mm^{-2} and $M=0.02$ mm^{-1} are the basis of the VESSEG validation with respect to an idealized saccular aneurysm with a radius of 50 mm. Figure 4 shows the mean and Gaussian curvatures predicted by VESSEG for the cylinder and sphere indicating excellent agreement with the analytical calculations throughout most of the surface geometry. The four second-order curvature-based indices were computed for both models and are shown in Table 2. The analytical calculation of these indices was performed using Eqs. (17)–(20), while the numerical predictions are those obtained using VESSEG with the respective surface meshes. The comparisons indicate absolute differences ranging from 0% to 2% between the numerical predictions and the analytical calculations, which are accounted for with the degree of mesh refinement in the models [14].

Table 2 Analytical and numerical values (predicted by VESSEG) of second-order curvature-based indices for the idealized geometries of a sphere and a cylinder (GAA is in (mm^{-1}), while MAA is in (mm^{-2}). Parentheses indicate absolute percentage difference of the numerical predictions with respect to the analytical calculations of the four curvature-based indices.)

	Sphere		Cylinder	
	Analytical	Numerical	Analytical	Numerical
GAA	0.00040	0.00039 (−0.001%)	0	5×10^{-8} (≈0%)
MAA	0.020	0.018 (−0.2%)	0.025	0.017 (−0.8%)
GLN	1.00	1.02 (+2%)	0	5×10^{-5} (0.005 %)
MLN	0.28	0.26 (−2%)	0.22	0.20 (−2%)

3.3 Geometrical Characterization of AAAs and Controls. The 3D patient-specific geometries were segmented and reconstructed from CT images of nine AAA subjects treated for elective repair at Allegheny General Hospital in Pittsburgh, PA (see Fig. 5). Also illustrated in this figure, an idealized aneurysm and a control subject (healthy abdominal aorta) were used to evaluate the various geometrical indices. The idealized geometry is a 3D axisymmetric fusiform-shaped aneurysm with a volume equal to the average volume of the nine patient-specific aneurysms (130 cm^3) and can therefore serve as a size-matched control. The analyses were conducted using identical meshing and smoothing protocols. All sizes, shapes, and curvature-based indices were computed for the eleven computer-generated 3D geometries and are shown in Table 3.

3.4 Application of the Wall Thickness Detection Algorithm. The wall thickness detection algorithm was tested by direct comparison with the discrete point measurements reported

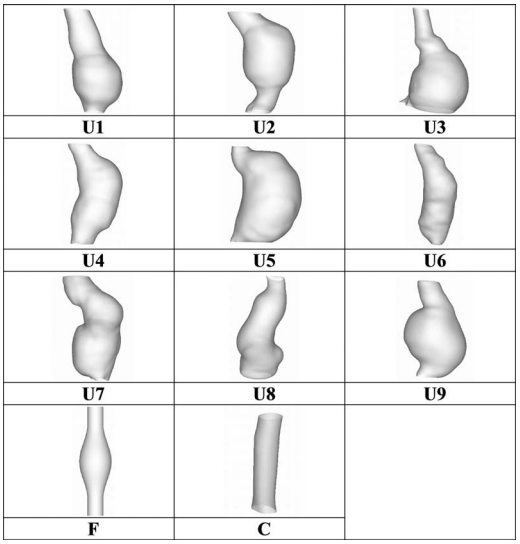

Fig. 5 Patient-specific AAA models (U1,…, U9), idealized fusiform-shaped AAA model (F) and patient-specific normal abdominal aorta model used as control (C).

Table 3 Geometrical indices for the patient-specific AAAs, control model, and fusiform aneurysm (All one-dimensional size indices are in (mm); the AAA volume (V) and the thrombus volume (V_{ILT}) are expressed in (cm^3), the surface area (S) is in (cm^2); GAA is in (mm^{-1}), while MAA is in (mm^{-2}))

	U1	U2	U3	U4	U5	U6	U7	U8	U9	C	F
One-dimensional size indices											
D_{max}	52.42	51.65	65.14	45.88	59.64	43.00	58.36	43.46	55.99	19.91	50
D_{neck1}	27.94	27.94	19.42	21.07	20.00	0	31.22	23.27	21.04	-	25
D_{neck2}	33.61	30.40	24.97	24.10	35.47	31.08	39.25	30.85	27.47	-	25
H	62.50	76.25	82.50	90.00	81.00	99.00	93.00	90.00	70.50	54	110
H_{neck}	32.50	2.50	17.50	6.00	3.00	0	18.00	9.00	25.50	-	30
L	70.38	89.19	104.37	102.19	107.86	114.88	103.16	105.47	85.61	54.44	110
L_{neck}	35.36	2.70	19.92	7.36	3.20	0	22.91	10.95	31.83	-	30
Hb	35.00	37.50	62.50	60.00	48.00	21.00	51.00	51.00	30	-	85
d_c	2.75	6.43	10.97	2.48	3.21	3.10	12.81	1.65	2.42	0	0
Two-dimensional shape indices											
DHr	0.84	0.68	0.79	0.51	0.74	0.43	0.63	0.48	0.79	0.37	0.45
DDr	1.56	1.70	2.61	1.90	1.68	1.38	1.49	1.41	2.04	-	2
Hr	1.92	30.50	4.71	15.00	27.00	0	5.17	10.00	2.76	-	3.67
BL	0.56	0.49	0.76	0.67	0.59	0.21	0.55	0.57	0.42	-	0.77
β	0.95	0.87	0.83	0.94	0.95	0.93	0.78	0.96	0.95	1	1
T	1.06	1.09	1.24	1.13	1.33	1.15	1.05	1.13	1.23	1	1
Three-dimensional size indices											
V	97.06	114.33	177.42	110.62	174.68	108.33	185.12	95.62	106.17	13.70	130
S	84.63	101.39	130.96	108.08	131.76	113.57	144.88	101.38	92.68	28.18	136
V_{ILT}	30.26	59.07	137.46	54.88	64.59	26.36	131.06	34.88	23.35	-	0
γ	0.31	0.52	0.77	0.50	0.37	0.24	0.71	0.36	0.22	-	0
Three-dimensional shape indices											
NFI	0.076	0.073	0.136	0.075	0.072	0.244	0.037	0.024	0.011	-	0
IPR	4.00	4.30	4.15	4.69	4.22	4.50	4.46	4.85	4.13	4.92	5.28
Second order curvature-based indices											
GAA	0.0008	0.0009	0.0015	0.0006	0.0014	0.0009	0.0014	0.0019	0.0015	0.0033	0.00006
MAA	0.049	0.050	0.049	0.047	0.042	0.051	0.048	0.063	0.049	0.074	0.029
GLN	5.20	8.67	8.83	5.51	7.70	6.16	8.05	6.83	5.45	2.60	4.45
MLN	0.44	0.49	0.55	0.44	0.46	0.45	0.55	0.54	0.49	0.25	0.33

by Raghavan et al. [22] with AAA No. 1 cadaver model. The post mortem CT images of this aneurysm underwent a segmentation, reconstruction, and meshing process identical to that of the 11 AAAs and controls. The 61 known wall thickness sites measured from eight tissue specimens dissected from the aneurysm were located in the 3D wall thickness distribution to probe the accuracy of the numerical predictions on a nodal basis, as shown in Fig. 6 for the left and right views of the model. The measured wall thicknesses were subsequently compared with the VESSEG numerical predictions for all 61 sites. The average relative difference in the wall thickness at these sites was calculated at 7.8% for the left (15 sites) and right (16 sites) views, respectively, of the numerically predicted arterial wall thickness, as reported in Table 4. In addition, our previous work on interobserver variability and reproducibility of the wall thickness detection algorithm indicates there is adequate repeatability among manual measurements made by two double-blinded VESSEG users [29]. In this investigation, wall thickness measurements showed good agreement between users with coefficients of variation ranging from 0.0% to 6.0% (for 10 ruptured aneurysms) and 0.1% to 6.6% (for 10 unruptured aneurysms).

3.5 AAA Wall Thickness. Figure 7 shows the local wall thickness distribution for models U1 and U5, illustrating the variability of this parameter (from 0.8 mm to 3.5 mm) in patient-specific AAAs. Wall thickness is shown in Fig. 8 as a function of axial position of the aneurysm sac for model U9. The renal arteries are taken as the point of reference for zero axial position while the maximum axial position (corresponding to the height of the aneurysm H) is located at the iliac bifurcation. Figure 9 illustrates the variation of the minimum and maximum wall thicknesses at each cross section as a function of axial position of the aneurysm sac for model U9. The circumferential distribution of wall thickness at the 72 perimeter points on the wall surface for the largest cross section of model U9 (where D_{max} is located) is shown in Fig. 10, which exemplifies the in-plane variability of the vessel wall of the diseased abdominal aorta.

4 Discussion

A reliable quantification of the shape and size of patient-specific AAAs carries several benefits; it may provide *individual* rupture and operative risks during presurgical planning, and it would be valuable in establishing index thresholds for patient selection and for customized designs of endovascular grafts. Likewise, local changes in wall thickness may play an important role in the wall mechanics and rupture potential.

Due to intersubject variability in the healthy infrarenal aorta diameter (1.5–2.5 cm), the common criterion of AAA maximum diameter may not be adequate for the assessment of rupture risk. Therefore, the patient-specific DDr index is proposed here as a more accurate parameter for personalized assessment of the aneurysm size. Cappeler et al. [33] confirmed that a reasonable threshold for elective repair and rupture risk prediction is $2.2 \leq \text{DDr} \leq 3.3$. In our cohort of AAAs, only one (U3) meets the proposed criteria for elective repair, having DDr equal to 2.61; U3 also has $D_{max}=65.14$ mm ($>D_{critical}=55$ mm).

Clinical studies demonstrate that 75% of AAAs contain thrombus [11]. The effect of thrombus concerning rupture risk assessment is controversial in the literature. Di Martino and Vorp [34]

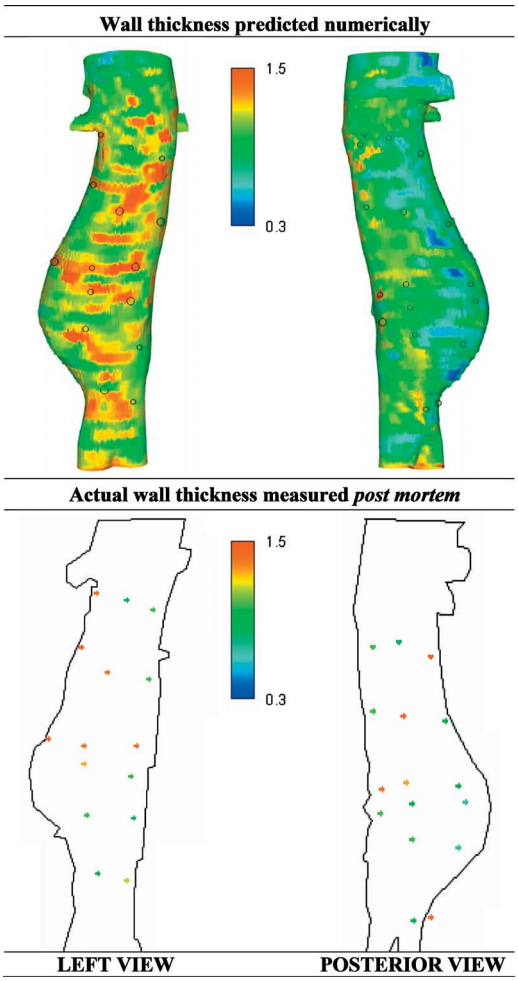

Fig. 6 Comparison of discrete wall thickness sites between VESSEG predictions and actual measurements from cadaver specimen AAA No. 1 reported by Raghavan et al. [22]

Table 4 Direct evaluation of discrete wall thickness sites predicted by VESSEG and a comparison with actual measurements from cadaver specimen AAA No. 1 reported by Raghavan et al. [22] The average relative difference between the post mortem and numerical predictions is 7.8%.

Left view	
Post mortem	Numerical
1.41	1.31
0.92	0.92
1.10	1.06
1.89	1.29
1.48	1.34
1.11	1.09
1.81	1.32
1.46	1.33
1.46	1.41
1.36	1.33
1.16	1.17
1.10	1.12
0.86	1.03
1.04	1.06
1.17	1.15
Posterior view	
1.10	1.10
0.92	0.91
1.62	1.05
1.11	1.09
1.74	1.10
1.01	0.99
1.46	1.45
1.33	1.16
0.97	0.95
1.16	1.14
0.97	0.98
0.82	0.86
1.11	1.11
0.81	0.82
1.00	1.02
1.39	1.16

showed that the presence of ILT reduces and redistributes the stresses in the aortic wall. In accordance with this study, Wang et al. [11] earlier demonstrated that the peak wall stress is reduced from 6% to 38% with an ILT volume ratio between 0.29 and 0.72. Conversely, Vorp et al. [35] reported that the presence of intraluminal thrombus could dramatically decrease the AAA wall strength; hypoxia caused by ILT is the main reason for this reduction. While Cappeler et al. [33] indicated that a value of $\gamma=0.62$ is a possible indicator for high rupture risk, the relation between ILT volume and aneurysm size seems to be contentious. In fact, according to a recent study [36], an increase in sac diameter did not correlate positively with an increase in ILT volume for large aneurysms (maximum transverse diameter larger than 7 cm). According to the maximum diameter criterion, patient models U3, U5, and U7 have the highest rupture potential. Models U3 and U7 exhibit the highest thrombus ratios, and they exceed the threshold for γ proposed by Cappeler et al. [33] as a rupture risk predictor.

Autopsy studies [12] show that ruptured AAAs are less fusiform rather than spherical. Therefore, the extent to which an aneurysm deviates from a fusiform shape may be a good indicator of rupture risk. Second order curvature-based indices are more complex and the physical meaning associated with them is not as evident. A local surface region with a positive Gaussian curvature indicates a surface with an elliptic region, while a negative Gaussian curvature indicates a hyperbolic region (also called gooseneck or saddle region), which can be subject to mechanical stress concentrations [28]. The area-averaged Gaussian curvature GAA and the area-averaged Mean curvature MAA are dependent on both size and shape, so their relative values become more important to interpret. For example, the relative value of MAA can be a measure of size in patients where we cannot appreciate a significant

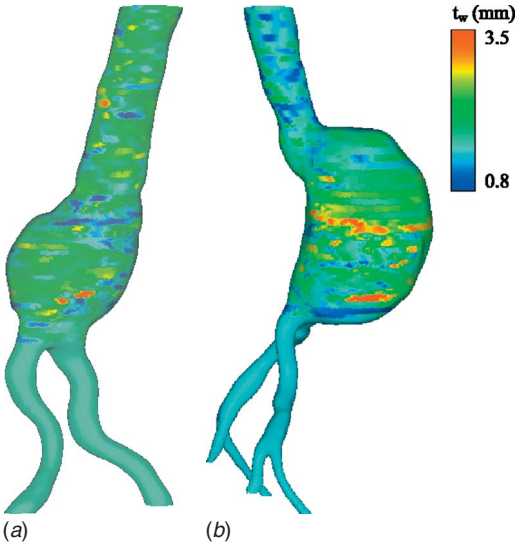

Fig. 7 Patient-specific wall thickness distributions for (*a*) U1 and (*b*) U5

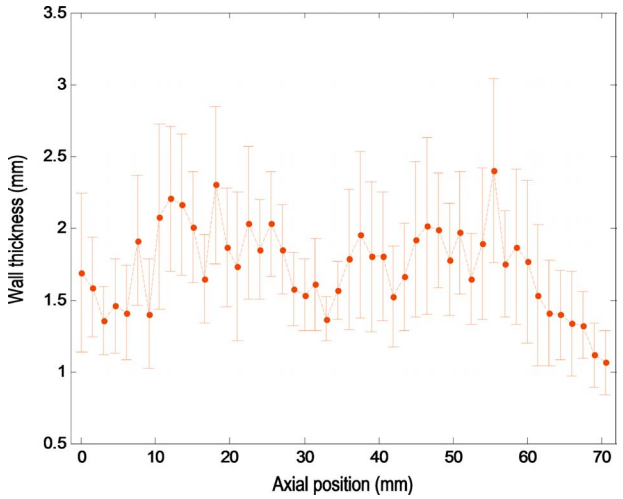

Fig. 8 AAA sac wall thickness (average with *Y* error bars) for model U9

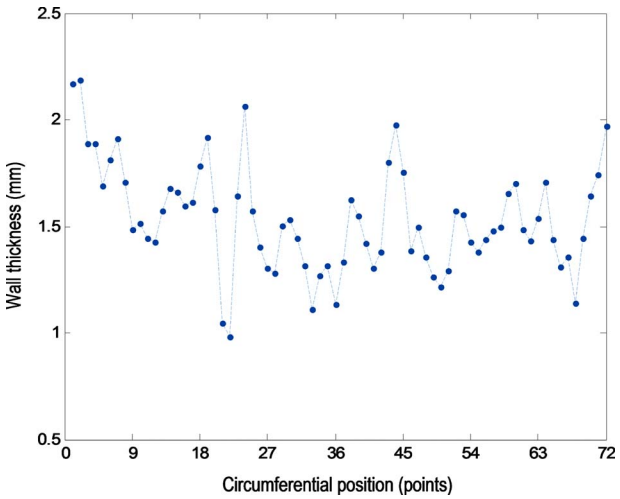

Fig. 10 Distribution of wall thickness at D_{max} cross section for model U9. The nonuniform circumferential spacing between points is approximately 5 deg

difference in shapes. Thus, MAA is larger for models U6 and U8 than for the other aneurysms, which is in accordance with U6 and U8 presenting a smaller maximum transverse diameter than the other models. Concerning the shape of an aneurysm, MAA indicates the existence of concave and convex regions on the aneurysm sac surface. While GAA and MAA exhibit a positive value for all models in this study (AAA and control), this does not translate into an absence of concave and gooseneck regions. These two indices provide an assessment of the global distribution of the surface curvature and do not quantify the individual complex local curvature changes. Therefore, global indices such as GAA and MAA should not be used to interpret the relative presence of local hyperbolic and concave regions on the surface of the AAA sac. Rather, the relative values of GAA and MAA can be used to compare AAAs. For example, considering two AAAs of comparable sizes (U6 and U8), U6 exhibits a smaller GAA and on its surface has more gooseneck regions compared with U8, which presents a larger GAA. GLN and MLN are dimensionless indices and their relative values can provide an indirect assessment of irregularities on the surface geometry. The larger the value of these indices the more irregular is the aneurysm surface. According to this, the controls (normal abdominal aorta and idealized fusiform aneurysm) yield the smallest GLN and MLN, while the presence of more surface irregularities in model U3 results in the highest GLN and MLN.

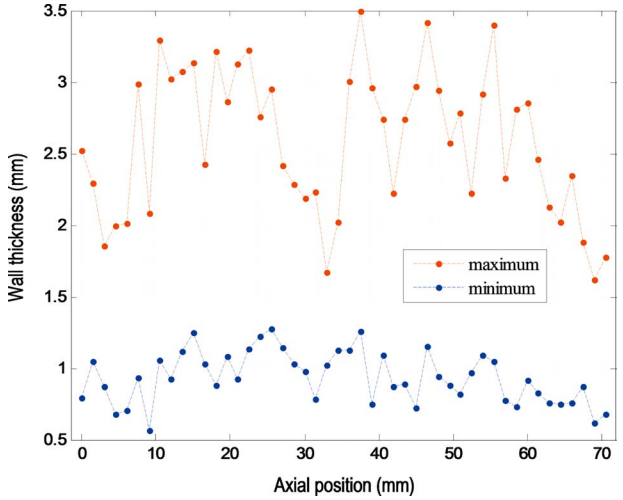

Fig. 9 Minimum and maximum AAA sac wall thickness for model U9

There are some limitations in our numerical quantifications of AAA shape and wall thickness. CT image resolutions with a pixel size of 0.7 mm do not allow for an accurate estimation of wall thickness less than this value and, therefore, VESSEG can only provide an approximate contour segmentation of the outer wall when the pixel size is as small as the local thickness of the blood vessel. Additionally, the procedure followed to validate the wall thickness algorithm (in lieu of using input from trained radiologists) has some inherent limitations. The cadaver model wall thickness measurements were obtained at a number of discrete points from excised rectangular tissue specimens as described by Raghavan et al. [22], which were superimposed on 2D boundary outlines of the AAA wall (see Fig. 6). The numerical evaluation of wall thickness is based on a different source of data: the CT images (without contrast enhancement) of the excised AAA (prior to removing the specimens) inflated at 100 mm Hg by inserting a balloon inside the abdominal aorta. Therefore, it is not surprising to find a difference of up to 7.8% between the post mortem measurements and the numerical predictions of wall thickness. Furthermore, the lack of higher image resolution leads to reconstructed surfaces with some unrealistic sharp corners where we applied a smoothing process to remove them. The same protocol of reconstruction and smoothing was employed on all the models and we assume that the genuine geometric features were not severely affected. Since the one-dimensional size indices, two-dimensional shape indices, and three-dimensional size and shape indices were computed directly from the patient-specific geometry, they are not affected by the reconstruction and smoothing protocol. However, the second-order curvature-based indices are more sensitive to smoothing, since they were calculated based on nodal coordinates of the final refined mesh. Finally, a limited number of nonruptured AAA subjects were used in this investigation; there is need to further validate the shape quantification method applying it to a larger population study that would also include ruptured AAAs.

Estimations of wall thickness are provided in the present study as a geometry-derived parameter and an addendum to the 3D geometrical characterization techniques based on size and shape. The noninvasive estimation of blood vessel wall thickness from medical image data is unprecedented for abdominal aortic aneurysms and, thus, extensive validation of the algorithms by trained radiologists will be necessary. These estimations are heavily depen-

dent on the use of a contrast medium, the image resolution, and the ability of the code to distinguish the outer wall surface from the fat and soft tissues enveloping the abdominal aorta. As seen in Figs. 6–10, there is a considerable in-plane variation of AAA wall thickness while only a moderate deviation in average thickness of any single cross section with respect to the overall average thickness of the AAA sac. The significance of this translates into highly localized regions of both thick and thin vascular tissues near the maximum transverse dimension (D_{max}). The development over time of heterogeneous multilayered intraluminal thrombi and pockets of calcification likely has an effect on the thickness variability of the vascular wall. Furthermore, this in-plane variation of AAA wall thickness is also a consequence of the segmentation and wall thickness detection algorithms, for which an error analysis was performed in our previous work [29].

Accurately quantifying the regional variations of wall thickness will be of paramount importance in the assessment of the AAA biomechanical environment. Comparable to ILT thickness, wall thickness appears to play a dual role in the evaluation of aneurysm rupture risk. On one hand, a thicker AAA wall may suggest severe inflammation of the AAA tissue and may indicate regions at higher risk of rupture. On the other hand, localized thin-walled regions are expected to exhibit stress concentration and therefore areas at high risk of rupture. Only an accurate characterization of all factors involved, including AAA shape, will lead to clinically relevant applications of AAA biomechanics. With radiologists and vascular surgeons making efficient use of CT imaging for presurgical planning and measuring AAA diameter over time during patient follow-ups, it is logical to question the importance of quantifying geometric characteristics that are observed in a qualitative manner by radiologists. For instance, it is not necessary to compute GLN and MLN to realize that model U3 has a more irregular surface than model U1. Visual inspection of the segmented and reconstructed AAA, a process that can be performed semi-automatically by most CT imaging commercial software in the radiology suite, can provide such qualitative assessment. However, quantification of parameters such as GLN and MLN, and the graphical mappings of K and M, offer information unattainable with simple visual inspection: a measure of the degree to which the AAA wall geometry is irregular.

It is unlikely that any one of the proposed indices alone would be a reliable index of rupture risk or a threshold for elective repair. Rather, the complete geometry and a positive correlation of a set of indices should be considered to assess the potential for rupture. With this quantitative parameter assessment, future research can be directed toward statistical analyses correlating the numerical values of these parameters with the risk of aneurysm rupture or intervention (surgical or endovascular). While this work does not provide direct insight into the possible clinical use of the geometric parameters, we believe it provides the foundation necessary for future efforts in that direction.

Acknowledgment

The authors would like to acknowledge the critical contribution of the following former undergraduate students to the VESSEG program coding: Leah Acker, B.S. Electrical Engineering, Grove City College; Gopal Patel, B.S., Electrical and Biomedical Engineering, Carnegie Mellon University; and Daniel Goldman, B.S., Mechanical and Biomedical Engineering, Carnegie Mellon University. Moreover, the authors wish to thank Dr. Medhavan Raghavan and Dr. Erasmo Simao da Silva for providing the CT images and raw wall thickness data of the cadaver AAA model used in the present work for validating VESSEG's wall thickness algorithm. Ms. Saundra Grant's contribution as research coordinator of the retrospective review of records of AAA patients at Allegheny General Hospital was invaluable to this study. No extramural funding agencies provided support for this work.

References

[1] Patel, M. I., Hardman, D. T. A., Fisher, C. M., and Appleberg, M., 1995, "Current Views on the Pathogenesis of Abdominal Aortic Aneurysms," J. Am. Coll. Surg., **181**, pp. 371–382.
[2] Brown, L. C., and Powell, J. T., The UK Small Aneurysm Trial Participants, 1999, "Risk Factors for Aneurysm Rupture in Patients kept Under Ultrasound Surveillance," Ann. Surg., **230**, pp. 289–297.
[3] Limet, R., Sakalihasan, N., and Albert, A., 1991, "Determination of the Expansion Rate and the Incidence of Rupture of Abdominal Aortic Aneurysms," J. Vasc. Surg., **14**, pp. 540–548.
[4] Lederle, F. A., Johnson, G. R., and Wilson, S. E., 1997, "Prevalence and Associations of Abdominal Aortic Aneurysms Detected Through Screening," Ann. Intern. Med., **126**, pp. 441–449.
[5] The UK Small Aneurysm Trial Participants, 1998, "Mortality Results for Randomized Controlled Trial of Early Elective Surgery or Ultrasonographic Surveillance for Small Abdominal Aortic Aneurysms," Lancet, **352**, pp. 1649–1655.
[6] Vorp, D. A., Raghavan, M. L., and Webster, M., 1998, "Mechanical Wall Stress in Abdominal Aortic Aneurysm: Influence of Diameter and Asymmetry," J. Vasc. Surg., **27**, pp. 632–639.
[7] Fillinger, M. F., Marra, S. P., Raghavan, M. L., and Kennedy, F. E., 2003, "Prediction of Rupture Risk in Abdominal Aortic Aneurysm During Observation: Wall Stress Versus Diameter," J. Vasc. Surg., **37**, pp. 724–732.
[8] Venkatasubramaniam, A. K., Fagan, M. J., Mehta, T., Mylankal, K. J., Ray, B., Kuhan, G., Chetter, I. C., and McCollum, P. T., 2004, "A Comparative Study of Aortic Wall Stress Using Finite Element Analysis for Ruptured and Non-Ruptured Abdominal Aortic Aneurysms," Eur. J. Vasc. Surg., **28**, pp. 168–176.
[9] Vande Geest, J. P., Wang, D. H., Wisniewski, S. R., Makaroun, M. S., and Vorp, D. A., 2006, "Towards a Noninvasive Method for Determination of Patient-Specific Wall Strength Distribution in Abdominal Aortic Aneurysms," Ann. Biomed. Eng., **34**, pp. 1908–1916.
[10] Dobrin, P., Baker, W., and Gley, W., 1984, "Elastolytic and Collagenolytic Studies of Arteries," Arch. Surg. (Chicago), **119**, pp. 405–409.
[11] Wang, D., Makaroun, M., Webster, M., and Vorp, D. A., 2002, "Effect of Intraluminal Thrombus on Wall Stress in Patient Specific Models of Abdominal Aortic Aneurysm," J. Vasc. Surg., **36**, pp. 598–604.
[12] Da Silva, E. S., Rodrigues, A., and De Tolosa, E. C., 2000, "Morphology and Diameter of Infrarenal Aortic Aneurysms: A Prospective Autopsy Study," Cardiovasc. Surg., **8**, pp. 526–532.
[13] Smith, A. D. C., 1999, "The Folding of the Human Brain: From Shape to Function," Ph.D. thesis, University of London, London, UK.
[14] Ma, B., Harbaugh, R. E., and Raghavan, M. L., 2004, "Three-Dimensional Geometrical Characterization of Cerebral Aneurysms," Ann. Biomed. Eng., **32**, pp. 264–273.
[15] Raghavan, M. L., Ma, B., and Harbaugh, R. E., 2005, "Quantified Aneurysm Shape and Rupture Risk," J. Neurosurg., **102**, pp. 355–362.
[16] Pappu, S., Dardik, A., Tagare, H., and Gusberg, R. J., 2008, "Beyond Fusiform and Saccular: A Novel Quantitative Tortuosity Index May Help Classify Aneurysm Shape and Predict Aneurysm Rupture Potential," Ann. Vasc. Surg., **22**, pp. 88–97.
[17] Fillinger, M., Racusin, J., and Baker, R., 2004, "Anatomic Characteristics of Ruptured Abdominal Aortic Aneurysm on Conventional CT Scans: Implications for Rupture Risk," J. Vasc. Surg., **39**, pp. 1243–1252.
[18] Finol, E. A., Keyhani, K., and Amon, C. H., 2003, "The Effect of Asymmetry in Abdominal Aortic Aneurysms Under Physiologically Realistic Pulsatile Flow Conditions," ASME J. Biomech. Eng., **125**, pp. 207–217.
[19] Fillinger, M. F., Raghavan, M. L., Marra, S., Cronenwett, J., and Kennedy, F. E., 2002, "In Vivo Analysis of Mechanical Wall Stress and Abdominal Aortic Aneurysm Rupture Risk," J. Vasc. Surg., **36**, pp. 589–597.
[20] Nyilas, R. D., Ng, S. M. L., Leung, J., and Xu, X. Y., 2005, "Towards a New Geometric Approach to Assess the Risk of Rupture of Abdominal Aortic Aneurysms Using Patient Specific Modeling," Proceedings of the 2005 Summer Bioengineering Conference, Vail, CO, Jun. 22–26.
[21] Di Martino, E. S., Bohra, A., Vande Geest, J. P., Gupta, N., Makaroun, M., and Vorp, D. A., 2006, "Biomechanical Properties of Ruptured Versus Electively Repaired Abdominal Aortic Aneurysm Wall Tissue," J. Vasc. Surg., **43**, pp. 570–576.
[22] Raghavan, M. L., Kratzberg, J., Castro de Tolosa, E. M., Hanaoka, M. M., Walker, P., and Simao da Silva, E., 2006, "Regional Distribution of Wall Thickness and Failure Properties of Human Abdominal Aortic Aneurysm," J. Biomech., **39**, pp. 3010–3016.
[23] Mower, W., Baraff, L., and Sneyd, J., 1993, "Stress Distribution in Vascular Aneurysms: Factors Affecting Risk of Aneurysm Rupture," J. Surg. Res., **55**, pp. 155–161.
[24] Scotti, C. M., Shkolnik, A. D., Muluk, S. C., and Finol, E. A., 2005, "Fluid-Structure Interaction in Abdominal Aortic Aneurysms: Effects of Asymmetry and Wall Thickness," Biomed. Eng. Online, **4**(64.
[25] Scotti, C. M., Jimenez, J., Muluk, S. C., and Finol, E. A., 2008, "Wall Stress and Flow Dynamics in Abdominal Aortic Aneurysms: Finite Element Analysis Vs. Fluid-Structure Interaction," Comput. Methods Biomech. Biomed. Eng., **11**(3), pp. 301–322.
[26] Shkolnik, A. D., Scotti, C. M., Amon, C. H., and Finol, E. A., 2005, "Computational Modeling of Abdominal Aortic Aneurysms: An Assessment of Rupture Potential for Presurgical Planning," *Biomechanics Applied to Computer Assisted Surgery*, Y. Payan, ed., Research Signpost, Kerala, India, pp. 243–260.

[27] Di Martino, E. S., Guadagni, G., Fumero, A., Ballerini, G., Spirito, R., Biglioli, P., and Redaelli, A., 2001, "Fluid-Structure Interaction Within Realistic Three Dimensional Models of the Aneurysmatic Aorta as a Guidance to Assess the Risk of Rupture of the Aneurysm," Med. Eng. Phys., **23**, pp. 647–655.
[28] Sacks, M. S., Vorp, D. A., Raghavan, M. L., Federle, M. P., and Webster, M. W., 1999, "In Vivo Three-Dimensional Surface Geometry of Abdominal Aortic Aneurysms," Ann. Biomed. Eng., **27**, pp. 469–479.
[29] Shum, J., DiMartino, E. S., Goldhammer, A., Goldman, D., Acker, L., Patel, G., Martufi, G., and Finol, E. A., "Semi-Automatic Vessel Wall Detection and Quantification of Wall Thickness in CT Images of Human Abdominal Aortic Aneurysms," Med. Phys., submitted.
[30] Finol, E. A., and Amon, C. H., 2002, "Flow-Induced Wall Shear Stress in Abdominal Aortic Aneurysms: Part I-Steady Flow Hemodynamics," Comput. Methods Biomech. Biomed. Eng., **5**(4), pp. 309–318.
[31] Hamann, B., 1993, "Curvature Approximation for Triangulated Surfaces," *Geometric Modeling*, G. Farin, H. Hagen, and H. Noltemeier, eds., Springer-Verlag, New York, pp. 139–153.
[32] Jinnai, H., Watashiba, H., Kajihara, T., Nishikawa, Y., Takahashi, M., and Ito, M., 2002, "Surface Curvatures of Trabecular Bone Microarchitecture," Bone, **30**, pp. 191–194.
[33] Cappeller, W. A., Engelmann, H., Blechschmidt, S., Wild, M., and Lauterjung, L., 1997, "Possible Objectification of a Critical Maximum Diameter for Elective Surgery in Abdominal Aortic Aneurysms Based on One- and Three-Dimensional Ratios," J. Cardiovasc. Surg. (Torino), **38**, pp. 623–628.
[34] Di Martino, E. S., and Vorp, D. A., 2003, "Effect of Variation in Intraluminal Thrombus Constitutive Properties on Abdominal Aortic Aneurysm Wall Stress," Ann. Biomed. Eng., **31**, pp. 804–809.
[35] Vorp, D. A., Lee, P. C., Wang, D. H., Makaroun, M. S., Nemoto, E. M., Ogawa, S., and Webster, M. W., 2001, "Association of Intraluminal Thrombus in Abdominal Aortic Aneurysm With Local Hypoxia and Wall Weakening," J. Vasc. Surg., **34**, pp. 291–299.
[36] Pillari, G. P., 2000, "Crescent Sign Origin and the Thrombus-to-Lumen Ratio in Abdominal Aortic Aneurysm," Radiology, **214**, p. 604.